

# A Social Force Model for Multi-Agent Systems With Application to Robots Traversal in Cluttered Environments\*

Chenxi Li, Weining Lu, Qingquan Lin, Litong Meng, Haolu Li, Bin Liang

**Abstract**—This letter presents a model to address the collaborative effects in multi-agent systems from the perspective of microscopic mechanism. The model utilizes distributed control for robot swarms in traversal applications. Inspired by pedestrian planning dynamics, the model employs three types of forces to regulate the behavior of agents: intrinsic propulsion, interaction among agents, and repulsion from obstacles. These forces are able to balance the convergence, divergence and avoidance effects among agents. Additionally, we present a planning and decision method based on resultant forces to enable real-world deployment of the model. Experimental results demonstrate the effectiveness on system path optimization in unknown cluttered environments. The sensor data is swiftly digital filtered and the data transmitted is significantly compressed. Consequently, the model has low computation costs and minimal communication loads, thereby promoting environmental adaptability and system scalability.

**Index Terms**—Distributed robot systems, multi-robot systems, path planning for multiple mobile robots or agents

## I. INTRODUCTION

Multi-agent systems (MASs) have drawn increasing research focus due to extensive applications. In contrast to individuals, MASs are capable of solving more complex problems and achieving system-level optimization through coordinated collaboration and expanded observation. This is evidenced by natural phenomena such as bird migration [1] and ant foraging [2]. Multi-agent path planning (MAPP) is a fundamental problem for applications, especially in unknown cluttered environments. An optimal system path should reflect the synergistic behavior of self-organization. The solution need to simultaneously balance computation cost, communication load, scalability, and environmental adaptability.

The critical challenge in MAPP is the manifestation of collaboration, including aggregation and repulsion among individuals. By studying the behavior of biological groups, existing research has developed a number of potential solutions. Centralized control methods [3] can uniformly coordinate the behavior of each agents. However, such methods are

\*This work is supported by the National Natural Science Foundation of China under Grants 92248304. (Corresponding author: Weining Lu.)

Chenxi Li, Qingquan Lin, Litong Meng and Bin Liang are with the Department of Automation, Tsinghua University, Beijing, 100084, China. (e-mail: lcx22@mails.tsinghua.edu.cn, linqq19@tsinghua.org.cn, menglt@ieee.org, liangbin@tsinghua.edu.cn).

Weining Lu is with the Beijing National Research Center for Information Science and Technology, Tsinghua University, Beijing, 100084, China. (e-mail: luwn@tsinghua.edu.cn).

Haolu Li is with the School of Mechanical and Electrical Engineering, Beijing Information Science and Technology University, Beijing, 100192, China. (e-mail: 2022020087@bistu.edu.cn).

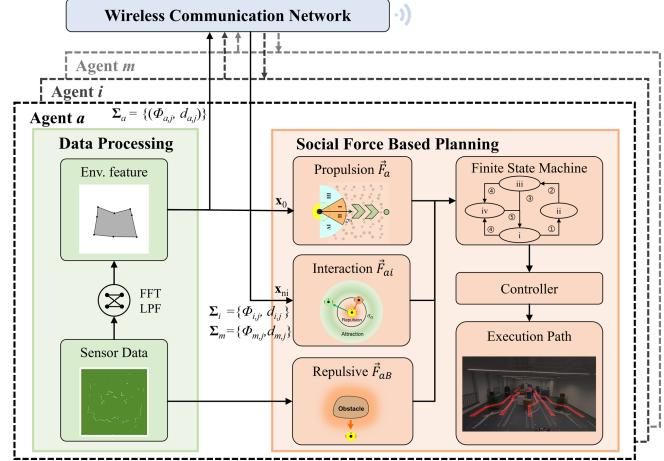


Fig. 1. System architecture. The Fast Fourier Transform (FFT) and Low-Pass Filtering (LPF) methods are available in our previous work [8].

challenging to implement in large-scale or communication-limited environments, as well as constrained in scalability due to computation costs. Distributed methods offer better adaptability and scalability. The current methods focus on either collision avoidance among trajectories [4], [5], or formation control [6], [7]. However, few works have managed to simultaneously coordinate the convergence and divergence behaviors through distributed control.

Humans possess a superior capacity for observation and autonomy. [9] presents social forces to measure the internal motivations of crowd individuals through the study of pedestrian motions. These forces elucidate the underlying causes of group behavior. Building upon the insights of [9], we propose a Social Force Model for Multi-Agent Systems (SFM-MAS). This model addresses the issue from the perspective of collaboration mechanism. The social forces enable MASs to exhibit the abilities of convergence, divergence, and avoidance. The environmental observations are fused with low computation costs and minimal communication loads. The model can be scaled to large swarms and deployed on micro, low-power robots. This letter makes the following contributions:

- The formulation of social forces is established, including the intrinsic propulsion, the interaction among agents, and the repulsion from obstacles. The observations of individual agents are enhanced through social force calculation, which results in spontaneous formation, path divergence and collision avoidance to optimize system paths.
- A finite state machine (FSM) is proposed for plan-

ning and decision in different resultant force scenarios, thereby enabling SFM-MAS to be deployed on robot swarms in the real world.

- The proposed SFM-MAS is applied to simulations and real-world experiments on robot swarms. The validity of system path optimization and environmental adaptability is demonstrated.

## II. RELATED WORKS

### A. Single Robot Local Planning

There have been plenty of studies focusing on single robot operating in unknown environments. A common solution is Simultaneous Localization and Mapping (SLAM) [10], [11]. However, due to limitations such as sensor drift, computation and power costs, SLAM is challenging to deploy in large scale scenarios [12]. Learning-based methods are capable of generalization in unknown environments [13], and some of them can directly map from observation to control [14], [15]. However, these methods require significant pre-training costs and lack theoretical security guarantees. Currently, some lightweight methods achieve local planning by imitating animal behaviors. For instance, the Bug algorithm [16], [17] and Potential Field (PF) methods [18], [19] emulate the reactive strategies of insects, while methods such as EGO-Planner [20] and FASTER [21], which optimize long-term trajectories, are more alike to the way of flying birds.

In the proposed SFM-MAS, the planning execution is similar to reactive strategies. However, by utilizing social forces, we facilitate observation fusion in MASs. Consequently, a system-level optimization for long-term planning is achieved.

### B. MAS Applications for Robot Swarms

The expansion from individual robots to MASs in real-world applications need to address two critical issues: collaboration and conflict. As for SLAM approaches, the system must achieve real-time alignment of point clouds. This places challenging demands on sensors, onboard computing and communication devices [22]. As for learning based methods, there are mainly two kinds of approaches currently. One kind describes the problem as sequential decision-making in system level. A typical approach is collision avoidance with deep reinforcement learning [23], which used safety constraints, target constraints, and kinodynamic constraints to prevent collisions. The other kinds focus on sensor-level planning [24], [25], which allow each system individuals to operate independently, thereby offering better scalability. However, learning-based methods face inherent issues, such as fixed neural network dimensions and sparse rewards in training, as well as challenges in real-world deployment [26]. In addition, these methods mainly address the issue of conflicts, but there is a lack of collaboration among robots.

The physical significance of bionic methods permits their extension to swarm applications. One kind of solution is the leader-follower method. For instance, [6] extends the Bug algorithm to robot formations through planning and control constraints. [7] proposes to optimize the trajectory of the leader based on the formation shape and size. Other

solutions involve sharing trajectories within a swarm, so as to improve the planning efficiency and reduce the risk of collision. For example, [27] employed the received signal strength intensity of an external beacon to facilitate dispersed paths, thereby enhancing the swarm efficiency in exploring unknown environments. [5] extended [20] to micro flying robots, achieving traversal and tracking in wild environments by joint optimization of spatial-temporal trajectories.

However, it is evident that the collaboration of current solutions is not yet comprehensive. Some focus on the convergence of the swarm, while others emphasize the dispersion among robots. The strategy of our work is similar to [3]. This work drew on the behavior of bird flocks, which introduced constraints for swarm convergence, repulsion, and velocity maintenance within a nonlinear model predictive control framework. Nevertheless, this method requires a central computing node, making it difficult to deploy in large outdoor areas. Additionally, the scalability of the system is limited by high demand for computing resource. In contrast, our proposed SFM-MAS solves the problem in a distributed way. The convergence, divergence, and avoidance of MASs are presented in a clear and concise manner. At the same time, the efficiency of computation and communication promotes the scalability and adaptability of the application.

## III. FORMULATION OF SFM-MAS

The proposed SFM-MAS comprises 3 parts. The intrinsic propulsion  $\vec{F}_a$  leads the agent  $R_a$  to the target. The interaction force  $\vec{F}_{ai}$  from neighbor  $R_i$  regulates convergence and divergence effects. And the repulsion force  $\vec{F}_{aB}$  keeps safety distances from obstacle borders. The above forces will be introduced in this section.

### A. Repulsion Force from Obstacles

In the real-world, agents have their collision volumes. We design a protective model in Fig. 2(a). This model employs a circle with a radius of  $r$  as the safety margin, so as to maintain a certain distance from obstacles. Let us consider an agent  $R_a$  with its target direction  $\vec{e}_a$ , and lateral width  $r_0$ . The central angle between points  $D$  and  $E$  is defined as the safety sector angle  $\alpha$ , and the length of  $\|OB\|$  is the planning distance  $l_{th}$ . From geometric relationships, we have:

$$\alpha = \pi - 2 \arccos\left(\frac{r_0}{r}\right), \quad (1)$$

$$l_{th} = \frac{r}{\cos\left(\frac{\pi-\alpha}{2}\right)} = \frac{r^2}{r_0}. \quad (2)$$

We use a potential field  $V_{aB}(\|\vec{r}_{aB}\|)$  to model the repulsion force. Let  $\vec{r}_{aB}$  denote the distance vector observed in the safety sector to the closest point of obstacle  $B$  (e.p.  $OB$  in Fig. 2(b)). Then, the repulsion force is expressed as:

$$\vec{F}_{aB}(\|\vec{r}_{aB}\|) = -\nabla_{\vec{e}_{aB}} V_{aB}(\|\vec{r}_{aB}\|), \quad (3)$$

where  $V_{aB}$  is a monotonically increasing potential, and  $\vec{e}_{aB}$  is a unit vector in the direction of  $\vec{r}_{aB}$ . An inverse

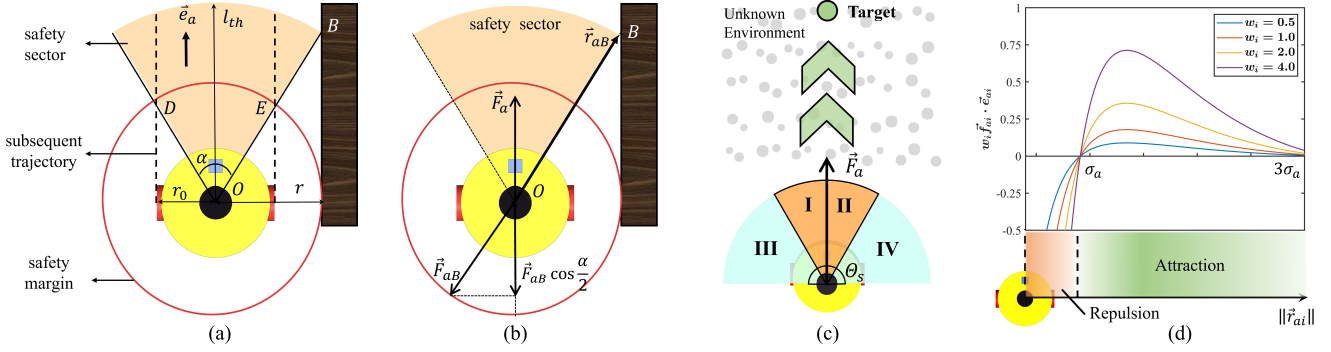


Fig. 2. (a) Agent Protective model. (b) Repulsion force from obstacles at the boundary of the safety sector. (c) Intrinsic propulsion and observation quadrants. (d) The magnitude curves of the interaction forces, where  $\sigma_a = 0.91m$  used in simulation.

proportional kernel is used to model the repulsive field:

$$V_{aB} = -\frac{V_{0B}}{\|\vec{r}_{aB}\|}, \vec{F}_{aB} = -\frac{V_{0B}}{\|\vec{r}_{aB}\|^2} \vec{e}_{aB}, \quad (4)$$

where  $V_{0B}$  is a constant. When the obstacle is at the boundary of the safety sector, the agent approaches the obstacle to the critical point (Fig. 2(b)). At this point,  $\|\vec{r}_{aB}\| = l_{th}$ ,  $\vec{F}_{aB}$  needs to completely balance the propulsion force  $\vec{F}_a$  in the direction of  $\vec{e}_a$  to avoid danger, so we have:

$$V_{0B} = \frac{l_{th}^2}{\cos(\frac{\alpha}{2})} \|\vec{F}_a\|. \quad (5)$$

### B. Intrinsic Propulsion

The objective of the agent  $R_a$  is to reach its target in the shortest and most stable manner possible. Therefore, the desired direction  $\vec{e}_a$  is directly towards the target. The field of view of the agent is defined as  $\Theta_s > \alpha$ . We divide the agent's observation area into four quadrants, as illustrated in Fig. 2(c). The front-left (I) and front-right (II) quadrants are divided by  $\vec{e}_a$ , splitting the safety sector into two halves. These two quadrants of observations are essential for safety. While the left-side (III) and right-side (IV) quadrants are analogous to the human afterglow. In most cases, agents only need to process the observations in front of them. We model the intrinsic propulsion of  $R_a$  as:

$$\vec{F}_a = w_a P_s \vec{e}_a, \quad (6)$$

where  $w_a$  is the weight coefficient, and  $P_s$  is the probability for a detour. When an obstacle is observed in the safety sector, the agent will select the detour direction according to its environmental observation. We define  $P_s$  as the probability of turning left. A sigmoid function  $\sigma[\cdot]$  is employed to map environmental observations to the probability domain:

$$P_s = \begin{cases} \sigma[\mathbf{W}_0^\top \mathbf{x}_0 + b_0] & \text{obstacle exist} \\ 0.5 & \text{no obstacle} \end{cases}, \quad (7)$$

with the estimated open space area  $\mathbf{x}_0$  and weight vector  $\mathbf{W}_0$  in the four quadrants.  $b_0$  is the bias entry. The absolute values of  $\mathbf{W}_0$  are symmetric but opposite in sign:

$$\mathbf{W}_0 = \frac{[w_s, 1, -1, -w_s]^\top}{(1 + w_s)}, \quad (8)$$

where  $w_s$  is the weight ratio of the observations within safety sector and the afterglow. In the experiments, we set  $w_s = 1$ .

### C. Interaction Forces Among Agents

In order for MASs to exhibit collective effects observed in human pedestrians, we employ a field approach to model the interaction forces among agents. Let us consider a case when agent  $R_a$  observes its neighbor  $R_i$ , and the distance vector between them is  $\|\vec{r}_{ai}\|$ . The potential  $V_{ai}$  of the interaction effect and the force field  $\vec{f}_{ai}$  can be expressed as:

$$V_{ai}(\|\vec{r}_{ai}\|) = V_{ai}^{att}(\|\vec{r}_{ai}\|) + V_{ai}^{rep}(\|\vec{r}_{ai}\|), \quad (9)$$

$$\vec{f}_{ai}(\|\vec{r}_{ai}\|) = -\nabla_{\vec{e}_{ai}} V_{ai}(\|\vec{r}_{ai}\|), \quad (10)$$

where  $V_{ai}^{att}$  and  $V_{ai}^{rep}$  represent the attractive and repulsive potentials, respectively. When the distance between agents is very close, the force manifests as repulsion, which rapidly decays to zero as  $\|\vec{r}_{ai}\|$  increases. Then, the force transitions to attraction, and finally slowly decays to zero as  $\|\vec{r}_{ai}\|$  further increases. To achieve this effect, we model the attractive potential with an exponential kernel and the repulsive potential with an inverse proportional kernel, given by:

$$V_{ai}^{att}(\|\vec{r}_{ai}\|) = V_0 e^{-\frac{\|\vec{r}_{ai}\|}{\sigma_a}}, V_{ai}^{rep}(\|\vec{r}_{ai}\|) = -\frac{\sigma_a}{\|\vec{r}_{ai}\|}, \quad (11)$$

where  $\sigma_a$  denotes the reference distance, marking the transition from repulsion to attraction. When  $\|\vec{r}_{ai}\| = \sigma_a$ ,  $\vec{f}_{ai} = \mathbf{0}$ , so  $V_0 = e$ . The interaction field can be expressed as:

$$V_{ai}(\|\vec{r}_{ai}\|) = e^{1 - \frac{\|\vec{r}_{ai}\|}{\sigma_a}} - \frac{\sigma_a}{\|\vec{r}_{ai}\|}, \quad (12)$$

$$\vec{f}_{ai}(\|\vec{r}_{ai}\|) = \frac{1}{\sigma_a} \left( e^{1 - \frac{\|\vec{r}_{ai}\|}{\sigma_a}} - \frac{\sigma_a^2}{\|\vec{r}_{ai}\|^2} \right) \vec{e}_{ai}. \quad (13)$$

In the application, agents will go through a variety of states. Therefore, it is essential to construct a segmentation function  $\vec{F}_{ai}$  that performs differently under varying circumstances. During advancing state,  $\vec{F}_{ai}$  serves a similar role to the repulsion  $\vec{F}_{aB}$ , which maintains a sufficient distance between agents. Additionally, when the agent encounters an obstacle, it should determine the direction of advancement based on the resultant force. At this point,  $\vec{F}_{ai}$  needs to incorporate observations from neighboring agents. This allows for fusion decision in probabilistic domain through the computation of social forces. To sum up, by incorporating

the weight  $w_i$  and the probability of following  $P_{ni}$ , we obtain the expression for the interaction force:

$$\vec{F}_{ai} = \begin{cases} w_i \vec{f}_{ai} & \text{advancing or avoiding} \\ w_i P_{ni} \vec{f}_{ai} & \text{fusion decision} \end{cases}. \quad (14)$$

The amplitude of  $w_i \vec{f}_{ai}$  is depicted in Fig. 2(d). When  $0 < \|\vec{r}_{ai}\| < \sigma_a$ , the interaction force behaves as repulsion to regulate the distance among agents. When  $\sigma_a < \|\vec{r}_{ai}\| < 3\sigma_a$ , the force is gravitational for fusion decisions. When  $\|\vec{r}_{ai}\| \geq 3\sigma_a$ , the force decays almost to 0. We define  $\|\vec{r}_{ai}\| \in (\sigma_a, 3\sigma_a)$  as the pass band for fusion decision. Neighboring agents outside the pass band are either too close or too far away, thus their observations do not contribute significantly to the decision process. We set  $P_{ni} = 0$  in such cases.

The connotation of  $P_{ni}$  is the probability to follow the neighbor.  $P_{ni}$  will be high if there are few obstacles observed by neighbor  $R_i$  towards the target of  $R_a$ . This will result in a strong attractive effect, thereby increasing the likelihood of  $R_a$  to follow it. Conversely, if the location of  $R_i$  is obstructed by obstacles,  $P_{ni}$  will be lower, leading a divergence effect. In such cases,  $R_a$  will be more likely to take a different path, which avoids the detours that would otherwise caused by blind following. Since there are only two cases of turns in 2D path planning,  $P_{ni}$  needs to be differentiated according to the relative orientation of the neighbors:

$$P_{ni} = \begin{cases} \sigma[1^\top \cdot (\mathbf{x}_{ni} + \mathbf{w}_n)] & \text{left neighbor} \\ 1 - \sigma[1^\top \cdot (\mathbf{x}_{ni} + \mathbf{w}_n)] & \text{right neighbor} \end{cases}, \quad (15)$$

where  $\mathbf{x}_{ni}$  and  $\mathbf{w}_n$  are both 2D vectors.  $\mathbf{x}_{ni}$  denotes the estimates of the passable distances in the direction of  $\vec{e}_a$ , quadrants I and II.  $\mathbf{w}_n$  is the thresholds. Since the observation of neighbor  $R_i$  relative to  $R_a$  is biased, the neighbor weight should be less than the weight of  $R_a$  itself. Hence, the values for  $w_i$  should satisfy  $\max \|w_i \vec{f}_{ai}\| < w_a$ .

#### IV. PLANNING AND DECISION BASED ON SFM-MAS

The social force model for pedestrians [9] treats human planning and reaction as an "automatic" process. However, agents require a more detailed method for planning and decision. In order to adapt the SFM-MAS to robot swarm applications, we propose a FSM of state transition, as illustrated in Fig. 3. In this section, we will elaborate on the states that robots are going through during a traversal task, and the model parameters correspond to robot dimensions.

##### A. Advancing Forward

For a robot  $R_a$ , when there are no obstacles within its safety sector, it will advance towards the target under its intrinsic propulsion  $\vec{F}_a$  (Fig. 3(b) AB). We assign model parameters based on the kinematic properties of the robot. Let us suppose the maximum velocity is  $v_m$ , the maximum acceleration is  $a_m$ , and the sensor delay is  $t_d$ . Consequently, the safety margin radius  $r$  can be expressed as:

$$r = r_e + v_m t_d + \frac{v_m^2}{2a_m}, \quad (16)$$

where  $r_e$  denotes the radius of the robot outer circle. The second term represents the sensor delay distance  $s_d$ , and the third term denotes the braking distance  $s_b$ . In order to keep the distances between robots greater than  $2r$ , we set:

$$\sigma_a = 2(r + s_d + s_b). \quad (17)$$

Thus, the collisions or disturbances among robots can be eliminated. Different from [18] or [19], robots independently calculate the repulsion force from each obstacle rather than their resultant force. This can avoid saddle points commonly encountered in PF methods. When the repulsion force from any obstacles in the direction of  $\vec{e}_a$  greater than the intrinsic propulsion, the robot must stop to avoid collisions:

$$\exists B \text{ in } \Theta_s, (\vec{F}_a + \vec{F}_{aB}) \cdot \vec{e}_a \leq 0, \quad (18)$$

and then, the robot change to fusion decision state.

##### B. Fusion Decision

The process of the fusion decision (Fig. 3(b) B) can be described as follows: First, the robot  $R_a$  requests and receives observations from all neighbors within its field of view. Then, it calculates the amplitudes of social forces, as well as the probabilities of its own and neighbor following. Finally,  $R_a$  makes a decision based on the resultant force, and chooses a direction to follow the current obstacle:

$$P(\text{left}) = \frac{1}{Z} \left( \|\vec{F}_a\| + \sum_{i, P_{ni} > 0} \|\vec{F}_{ai}\| \right), \quad (19)$$

$$Z = w_a + \sum_{i, P_{ni} > 0} (w_i \|\vec{f}_{ai}\|), \quad (20)$$

where  $P(\text{left})$  is the probability to turn left for a detour, and  $Z$  is a normalisation factor. Since there are only two possible directions, namely left and right, we consider the amplitudes of social forces as weights for probabilities, thus enabling scalar calculations in the probability domain. Ultimately, the robot selects the direction based on  $P(\text{left})$ .

In order to reduce computation and communication costs, we utilise methods in our previous work [8]. The FFT and digital LPF are employed to obtain azimuth-distance observations with smooth boundaries in polar coordinates. The cutoff frequency of the filter is equivalent to the safety sector angle  $\alpha$ . Then, the filtered data is subjected to a calculation of extrema, which yields the environmental features of robot  $R_i$  denoted by  $\Sigma_i$ . The computation costs are significantly reduced by FFT, and the processing delays are lowered to microsecond level. The feature  $\Sigma_i$  contains the extrema distances and azimuths, with the number of extrema  $N_i$  situated around  $(\Theta_s/\alpha)$ . Consequently, the data volume for transmission is only at the byte level:

$$\Sigma_i = \{(\phi_{i,j}, d_{i,j}) | j = 1, 2, \dots, N_i\}, \quad (21)$$

where  $\phi_{i,j}$  and  $d_{i,j}$  represent the azimuths and distances of the extrema, respectively. The direction of the maxima indicates more open space, while the direction of the minima indicates potential obstacles. Afterwards, all the vertices of



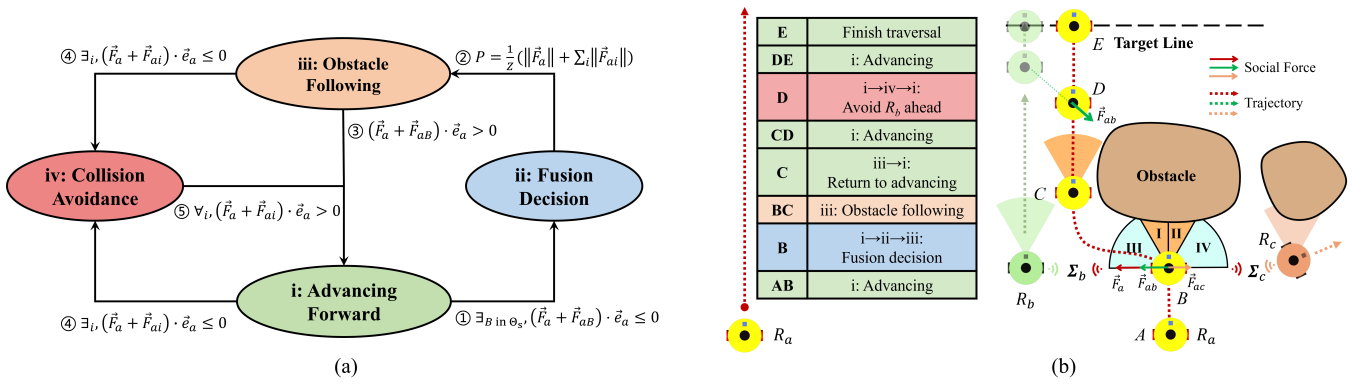


Fig. 3. (a) Finite state machine. (b) An example for SFM-MAS based planning and decision. This figure illustrates the process of robot  $R_a$ .

the extrema are connected to form a polygon, which represents an approximate observation reconstruction received from the neighbor  $R_i$ . Subsequently, a fuzzy evaluation is employed to assign the input of  $P_{ni}$ . If the reconstructed polygon contains minima within quadrants I and II, this indicates the possible presence of obstacles. Therefore,  $\mathbf{x}_{ni}$  is assigned as the average of the minimum and maximum values. Otherwise,  $\mathbf{x}_{ni}$  is assigned as the maximum extrema or boundary value of the quadrant:

$$\mathbf{x}_{ni,k} = \begin{cases} \max_k \{d_{i,k}\} & \text{no minima} \\ \text{avg}(\max_k \{d_{i,k}\}, \min_k \{d_{i,k}\}) & \text{minima exist} \end{cases}, \quad (22)$$

where  $k = 1, 2$ , denotes the safety sector in the target direction of robot  $R_a$ . As for the threshold  $w_n$  in (15), it is assigned as twice the total length of the protective model:

$$\mathbf{w}_{n,k} = 2(r + l_{th}) + s_d + s_b, k = 1, 2. \quad (23)$$

The same methodology is employed to process the robot's own sensor data. The dimensions of  $\mathbf{x}_0$  are defined as the areas of the polygon falling within the observation quadrants:

$$x_{0,k} = \sum_{j=0}^{n_k} \frac{1}{2} d_{0,j} d_{0,j+1} \sin(\phi_{0,j+1} - \phi_{0,j}), k = 1, 2, 3, 4 \quad (24)$$

where  $n_k$  represents the number of extrema within the robot's  $k$ -th observation quadrant. The values for  $j = 1$  to  $n_k$  indicate the extrema within the quadrant, while for  $j = 0$  and  $j = n_{i+1}$  represent the values of quadrant boundaries.

Finally, in the applications, we normalise the distance observation using the following function:

$$f_n[d] = \frac{d}{R} + 1, \quad (25)$$

where  $R$  is the observation range. The function  $f_n[d]$  shifts the value of  $d_{i,j}$  from  $[0, R]$  to  $[1, 2]$  to circumvent the issue in (24) when the value of  $d_{i,j}$  happens to be less than zero after non-linear FFT filtering. It is necessary to employ the same  $f_n[d]$  when calculating the result of  $\mathbf{w}_{n,k}$  in (23).

### C. Obstacle Following

In the obstacle following state, robot seeks a safety sector  $\vec{e}'_a$  closest to  $\vec{e}_a$  that meets the requirement of the protective model along the chosen direction. The robot then proceeds

towards  $\vec{e}'_a$  along the obstacle boundary (Fig. 3(b) BC). The effect of the propulsion  $\vec{F}_a$  will draw the direction of  $\vec{e}'_a$  close to  $\vec{e}_a$ , while the repulsion  $\vec{F}_{aB}$  will maintain a safe distance from the obstacle. When the robot meets the condition that:

$$\forall B \text{ in } \Theta_s, (\vec{F}_a + \vec{F}_{aB}) \cdot \vec{e}_a > 0, \quad (26)$$

it has successfully circumnavigated the obstacle. Then, it resumes to advance towards the target.

### D. Collision Avoidance

In order to prevent conflicts among robots, our model incorporates a collision avoidance state. When a robot is subjected to any repulsion  $\vec{F}_{ai}$  from neighbors greater than its own propulsion, the robot then enters the collision avoidance state (Fig. 3(b) D). The conditions can be express as:

$$\exists i, (\vec{F}_{ai} + \vec{F}_a) \cdot \vec{e}_a \leq 0, \quad (27)$$

In such circumstances, robot  $R_a$  will wait for its neighbor to pass until  $\vec{F}_{ai}$  is insufficient to counteract  $\vec{F}_a$ . In the event of two nearby robots yield simultaneously, the robot with the higher priority will exit and resume to advance forward. The priority of robots can be set according to application scenarios. In traversal tasks, we set higher priority to those relatively ahead to avoid robots in front getting the way.

## V. SIMULATION RESULTS

In this section, SFM-MAS is implemented for robot swarm traversal in complex unknown environments. To demonstrate the adaptability, we tested with swarms of 15 robots in both forest and rocky environments using Gazebo platform. The size of the environment is 20m by 20m, and the density of obstacles is about 1 per 5 square meters. The robot radius is  $r_0 = 0.15\text{m}$ , and its kinematic properties are:  $v_m = 0.5\text{m/s}$ ,  $a_m = 2\text{m/s}^2$ . It has a 5.5Hz LiDAR which observation range is  $R = 5\text{m}$ . We set the protection radius  $r = 0.30\text{m}$ , planning distance  $l_{th} = 0.60\text{m}$ , and safety sector angle  $\alpha = 60^\circ$ .

To ensure the test validity, 20 maps are randomly generated for each kind of environments. We compare the performance of SFM-MAS with 2 baselines: DH-Bug [17] and SFM-I (SFM-MAS in individual agent mode). As for DH-Bug baseline, the planning step is set to  $l_{th}$ . Additionally, in the events of no safe direction in the field of view, robots will randomly choose a direction to follow the obstacle. As

for SFM-I, the neighbor weight  $w_i$  is set to zero. This can demonstrate the performance improvement from interaction forces.

To evaluate the performance, we use the following statistical metrics: (a) Success weighted by inverse Path Length (SPL) [28], defined as the ratio of the optimal path to actual path length weighted by success rate. The closer SPL is to 1, the closer the execution path is to the optimal path. Here, we use the A\* [29] path as the optimal path, with a resolution of 0.05m. (b) Task duration time  $t_0$  for traversal. (c) Number of fusions  $N_u$ . (d) Number of planning failures  $N_a$ .

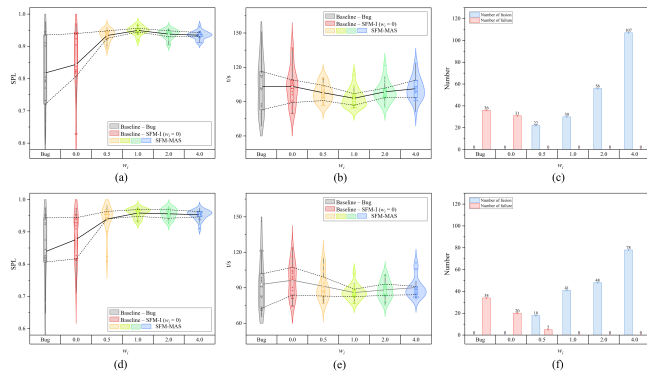


Fig. 4. Simulation statistics results. (a)-(c) and (d)-(f) show the performances in the forest and rocky environments, respectively.

TABLE I

STATISTICAL RESULTS OF SFM-MAS AND BASELINES IN SIMULATION

Env.	Algorithm	SPL (%)	$t$ (s)	$N_u$	$N_a$
Forest	DH-Bug	81.7	103.3	0	36
	SFM-I( $w_i = 0$ )	84.4	103.4	0	31
	<b>SFM-MAS(<math>w_i = 1.0</math>)</b>	<b>94.9</b>	<b>93.0</b>	<b>30</b>	<b>0</b>
Rocky	DH-Bug	83.8	92.9	0	34
	SFM-I( $w_i = 0$ )	87.6	96.4	0	20
	<b>SFM-MAS(<math>w_i = 1.0</math>)</b>	<b>95.8</b>	<b>86.0</b>	<b>41</b>	<b>0</b>

Fig. 4 and Table I show the performance statistics in simulations. The results demonstrate that SFM-MAS exhibits statistically significant improvements in terms of execution path and task duration. Additionally, there is a notable reduction in performance variance across different random maps. This indicates that SFM-MAS is capable of optimizing system paths through local observations. The average SPL performance of SFM-MAS reached 94.9% and 95.8% in forest and rocky environments, respectively, which are very close to the optimal paths. Furthermore, SFM-MAS effectively enhances the success rate of planning. The statistical results indicate the existence of numerous planning failures in the two baselines. This is mainly due to path overlaps among robots, leading to collision or interference. SFM-MAS addresses these issues by incorporating interaction forces among robots, thereby resulting in successful planning for all robots in the simulation.

Additionally, in the case of SFM-I, the paths of individual robots are optimized independently. The improvement in

this scenario is very slight in terms of average performance and variance. This is because the paths of robots are often interrelated. The decoupling of a system for optimization does not eliminate the possibility of interference, nor does it result in the collaborative effects. Hence, the significant role of interaction forces  $\vec{F}_{ai}$  in system planning process is demonstrated.

The statistical results also allow us to analyze the impact of the model parameter  $w_i$  on the performance.  $w_i$  is a weight coefficient that regulates the attraction and repulsion behaviors by altering the magnitude of  $\vec{F}_{ai}$ . If the value of  $w_i$  is excessively large, although the fusion count  $N_u$  increases, the system performance may even decline. This is because the observations of neighbors are biased, and a high  $w_i$  may introduce too many ineffective or incorrect observations. Conversely, if the value of  $w_i$  is too low,  $\vec{F}_{ai}$  will be too weak, which in turn leads to insufficient fusion and inadequate repulsion. This makes it challenging to generate the effect of synergy, and the system eventually degenerates to the SFM-I.

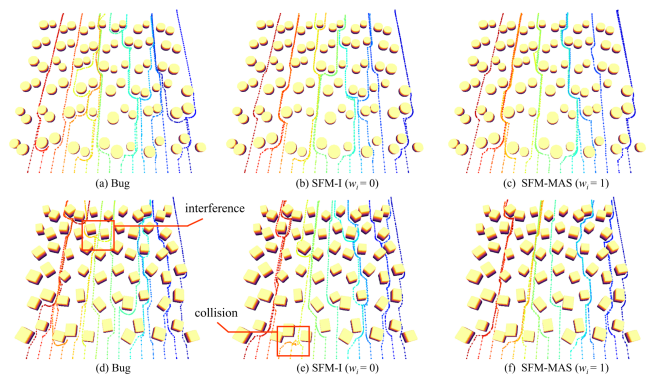


Fig. 5. The convergence effects of SFM-MAS. (a)-(c) and (d)-(f) illustrate the results of a random map in the forest and rocky environments.

Here, we illustrate the impact of social forces on system path optimization through two examples. In the first example, social forces create a convergence effect, with a formation spontaneously formed, as shown in Fig. 5. From the right-most column (c)&(f), it can be seen a clear convergence effect in SFM-MAS execution paths: When a robot finds a safe gap with fewer obstacles, it attracts nearby neighbor robots to follow its path. As a result, local groups (from 2 to 4 robots in the figure) are naturally formed along paths with relatively fewer obstacles. In contrast, the paths collision and interference can be observed in the two baselines. Overall, the convergence effect from SFM-MAS leads to smoother and more organized execution paths.

The second example illustrates the divergence effects in Fig. 6. The first row shows an example in a forest environment. Initially, Robot A follows Robot B. Then, Robot A encounters an obstacle and enters the fusion decision state. At this point, there is an obstacle at Robot B's location that needs to be detoured, so Robot B delivers a lower probability of following. In the meantime, Robot C observes a free space nearby, leading a higher following probability. Ultimately, Robot A decides to follow the direction of Robot C. The

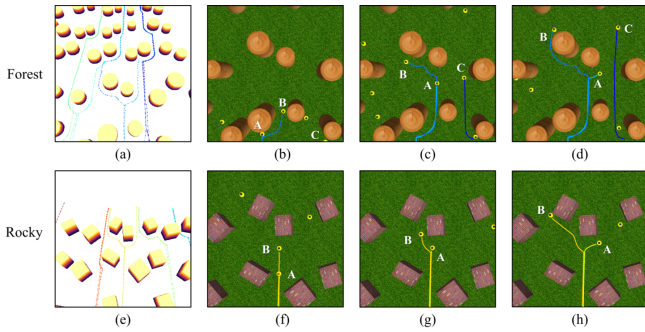


Fig. 6. The divergence effects of SFM-MAS. The leftmost figure in each row represents the final trajectory, and the figure on the right side shows the generation process as the robots advancing.

second row depicts a similar example in a rocky environment. As we can see, the effect of path divergence is also capable of optimising the system path. And this effect is achieved through the effective utilization of neighbor observations.

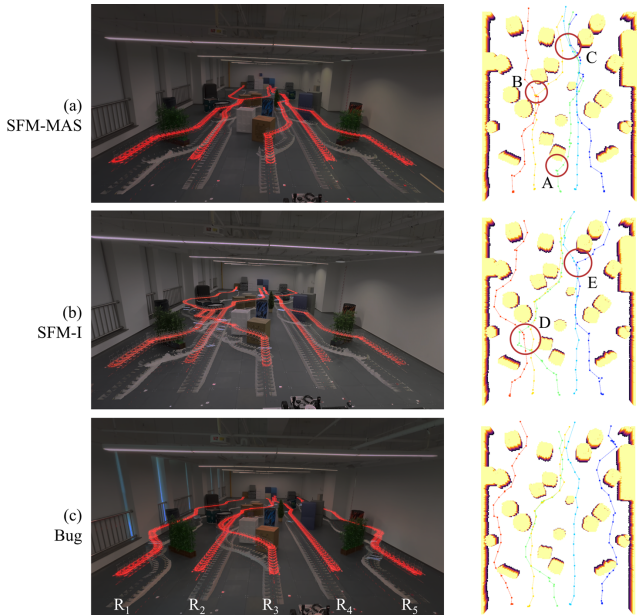


Fig. 7. Results in real-world experiments.

## VI. REAL WORLD EXPERIMENTS

Besides simulations, we also conducted real world experiments with a group of 5 robots. Each robot is equipped with an 8-core ARM v8.2 CPU and a 20Hz OS1 LiDAR with an effective range of 5m. Data transmission is performed by a 78.125 Kbps ultra wide band (UWB) module. The robots utilize AHD720P cameras and UWB ranging for mutual positioning, and employ CMP10A electronic compasses to determine relative orientation. The lateral collision distances is  $r_0 = 0.29\text{m}$ , and the external circular radius is  $r_e = 0.43\text{m}$  when rotating in place. The maximum speed is  $0.5\text{m/s}$ , and the acceleration is  $4\text{m/s}^2$ . Consequently, we set  $r = 0.49\text{m}$ ,  $l_{th} = 0.83\text{m}$ , and  $\alpha = 72^\circ$ . The LiDAR data is represented as a polar coordinate array with a length of approximately 360 points. We employ a FFT operation with  $n = 1024$  points to process the observation data in the fusion decision state. The

time complexity is  $O(n \log(n))$ , and the processing delay under our hardware conditions is only about  $13\mu\text{s}$ . As for communication loads, the environmental features are only transmitted in the fusion process. An example of the transmitted data  $\Sigma_i$  is shown in Table II. The data volume is only 48 to 64 bytes for each robot, and the transmission delay is less than 7ms under experimental conditions. Consequently, SFM-MAS is a lightweight model, capable to deploy on low-computation robots, or in communication-limited scenarios.

TABLE II  
AN EXAMPLE FOR SFM-MAS FUSION DECISION

Robot	$\Sigma_i$ in R3 Coord	$P_s$ or $P_{ni}$	$\ \vec{F}_a\ $ or $\ \vec{f}_{ai}\ $
R3	[[54, 1.62], [83, 1.53], [128, 1.78], [177, 1.55], [231, 1.89], [282, 1.55], [302, 1.58], [359, 1.18]]	0.504	0.504
R1	[[54, 1.17], [102, 1.44], [134, 1.39], [275, 1.89], [350, 1.47], [354, 1.47]]	0.395	0.236
R2	[[15, 1.60], [43, 1.67], [117, 1.24], [179, 1.83], [285, 1.03], [341, 1.77]]	0.581	0.279
R4	[[8, 1.78], [109, 1.17], [176, 1.85], [237, 1.27], [300, 1.69], [329, 1.62]]	0.403	0.266
R5	[[6, 1.28], [90, 1.84], [130, 1.65], [162, 1.76], [270, 1.17], [319, 1.76]]	0.414	0.247

The tested environment is cluttered and unknown. In order to facilitate the presentation of experimental results, a point cloud map was constructed by SLAM after all experiments finished. We used 4 external UWB stations to record the trajectories of each robot. The experimental results are illustrated in Figure 7. It is obvious that the path generated by SFM-MAS is better than the two baselines. The average path length of the SFM-MAS is 10.77m, with an SPL of approximately 96.2%. In contrast, the SFM-I and Bug baselines are 11.33m, 91.4% and 11.29m, 91.7%, respectively. In particular, we observed significant optimization at points A, B, and C. Figure 8 illustrates an example of decision fusion at point A. And Table II records the corresponding environmental features  $\Sigma_i$ , the probabilities, and the magnitudes of the social forces. Prior to fusion, the probability of robot  $R_3$  to turn left was  $0.504 > 0.5$ , while after fusion it became 0.478. Consequently, thanks to SFM-MAS fusion decision,  $R_3$  ultimately chose to proceed in a rightward direction, where the obstacles were fewer in number. Besides, point B demonstrated the divergence effect of the robot path, while point C demonstrated the convergence effect. These effects were achieved through the transmission of observations, the calculation of social forces, and the implementation of fusion decisions.

The optimization of the system paths also manifested in the repulsion and avoidance among robots. As illustrated in Figure 8(b), the interference is evidently occurred at points D and E in the SFM-I baseline. In contrast, at point C, despite four robots passing through successively, no interference was



observed due to the repulsion and collision avoidance. This demonstrates the optimization effect of  $\|\vec{F}_{ai}\|$  on the system path by regulating the distances between robots. This result further corroborates the conclusion: in the case of dense robots or obstacles, optimizing the path of individual robots independently is insufficient to improve system performance. Collaborative planning is necessary for the system.

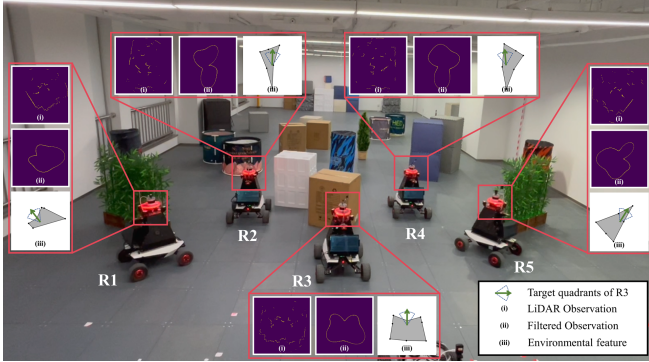


Fig. 8. An illustrative example of SFM-MAS fusion decision.

## VII. CONCLUSION

In this letter, we propose a Social Force Model for Multi-Agent Systems (SFM-MAS), and apply the model to robot swarm traversal in cluttered environments. This model addresses the problem of collaborative path planning from the perspective of fusion mechanisms. The SFM-MAS includes intrinsic propulsion, interaction among agents, and repulsion from obstacles. To enable the deployment of SFM-MAS in the real world, we developed a protection model and an observation model corresponding to the agent dimensions, as well as a FSM controlled by social forces. Simulation and real-world experiments demonstrate the effectiveness in achieving convergence, divergence and avoidance among agents within the system. Our future work includes the smoothness and continuity of trajectories, as well as testing on high-speed robots such as unmanned aerial vehicles.

## REFERENCES

- [1] C. W. Reynolds, "Flocks, herds and schools: A distributed behavioral model," *ACM Siggraph Computer Graphics*, vol. 21, no. 4, pp. 25–34, 1987.
- [2] C. Anderson, G. Theraulaz, and J. L. Deneubourg, "Self-assemblages in insect societies," *Insect. Soc.*, vol. 49, no. 2, pp. 99–110, 2002.
- [3] E. Soria, F. Schiano, and D. Floreano, "Predictive control of aerial swarms in cluttered environments," *Nat. Mach. Intell.*, vol. 3, no. 6, pp. 545–554, 2021.
- [4] X. Zhou, J. Zhu, H. Zhou, C. Xu, and F. Gao, "Ego-swarm: A fully autonomous and decentralized quadrotor swarm system in cluttered environments," in *2021 IEEE International Conference on Robotics and Automation (ICRA)*, Xi'an, China, 2021, pp. 4101–4107.
- [5] X. Zhou, X. Y. Wen, Z. P. Wang, Y. M. Gao, H. J. Li, Q. H. Wang, T. K. Yang, H. J. Lu, Y. J. Cao, C. Xu, and F. Gao, "Swarm of micro flying robots in the wild," *Sci. Robot.*, vol. 7, no. 66, p. 17, 2022.
- [6] W. N. Lu, T. Zhang, J. Yang, and X. Q. Wang, "A formation control approach with autonomous navigation of multi-robot system in unknown environment," in *34th Chinese Control Conference (CCC)*, NEW YORK, 2015, Conference Proceedings, pp. 5230–5234.
- [7] K. Ze, W. Wang, K. Liu, and L. J., "Time-varying formation planning and distributed control for multiple uavs in clutter environment," *IEEE Trans. Ind. Electron.*, pp. 1–11, 2023.

- [8] C. Li, W. Lu, Z. Ma, L. Meng, and B. Liang, "Highly efficient observation process based on fft filtering for robot swarm collaborative navigation in unknown environments," 2024.
- [9] D. Helbing and P. Molnár, "Social force model for pedestrian dynamics," *Phys. Rev. E*, vol. 51, no. 5, pp. 4282–4286, 1995.
- [10] M. Montemerlo, S. Thrun, D. Koller, B. Wegbreit, and Aaai, "Fast-slam: A factored solution to the simultaneous localization and mapping problem," in *Proc. of the AAAI Conference on Artificial Intelligence*, 2002.
- [11] T. Qin, P. Li, and S. Shen, "Vins-mono: A robust and versatile monocular visual-inertial state estimator," *IEEE Trans. Robot.*, vol. 34, no. 4, pp. 1004–1020, 2018.
- [12] Y. Dai, "Research on robot positioning and navigation algorithm based on slam," *Wirel. Commun. Mob. Comput.*, vol. 2022, p. 10, 2022.
- [13] A. Loquercio, E. Kaufmann, R. Ranftl, M. Muller, V. Koltun, and D. Scaramuzza, "Learning high-speed flight in the wild," *Sci. Robot.*, vol. 6, no. 59, p. 16, 2021.
- [14] S. Jung, S. Hwang, H. Shin, and D. H. Shim, "Perception, guidance, and navigation for indoor autonomous drone racing using deep learning," *IEEE Robot. Autom. Lett.*, vol. 3, no. 3, pp. 2539–2544, 2018.
- [15] W. Zhu and M. Hayashibe, "A hierarchical deep reinforcement learning framework with high efficiency and generalization for fast and safe navigation," *IEEE Trans. Ind. Electron.*, vol. 70, no. 5, pp. 4962–4971, 2023.
- [16] V. J. Lumelsky and A. A. Stepanov, "Path-planning strategies for a point mobile automaton moving amidst unknown obstacles of arbitrary shape," *Algorithmica*, vol. 2, no. 1-4, pp. 403–430, 1987.
- [17] Y. Zhu, T. Zhang, L. Y. Song, and X. Q. Li, "A new bug-type navigation algorithm for mobile robots in unknown environments containing moving obstacles," *Ind. Robot.*, vol. 39, no. 1, pp. 27–39, 2012.
- [18] O. Khatib, "Real-time obstacle avoidance for manipulators and mobile robots," in *Proc. 1985 IEEE International Conference on Robotics and Automation*, vol. 2, 1985, pp. 500–505.
- [19] S. G. Loizou and E. D. Rimon, "Mobile robot navigation functions tuned by sensor readings in partially known environments," *IEEE Robot. Autom. Lett.*, vol. 7, no. 2, pp. 3803–3810, 2022.
- [20] X. Zhou, Z. Wang, H. Ye, C. Xu, and F. Gao, "Ego-planner: An esdf-free gradient-based local planner for quadrotors," *IEEE Robot. Autom. Lett.*, vol. 6, no. 2, pp. 478–485, 2021.
- [21] J. Tordesillas, B. T. Lopez, M. Everett, and J. P. How, "Faster: Fast and safe trajectory planner for navigation in unknown environments," *IEEE Trans. Robot.*, vol. 38, no. 2, pp. 922–938, 2022.
- [22] K. Ebadi, L. Bernreiter, H. Biggie, G. Catt, Y. Chang, A. Chatterjee, and C. E. Denniston, "Present and future of slam in extreme environments: The darpa sub challenge," *IEEE Trans. Robot.*, vol. 40, pp. 936–959, 2024.
- [23] M. Everett, Y. F. Chen, and J. P. How, "Collision avoidance in pedestrian-rich environments with deep reinforcement learning," *IEEE Access*, vol. 9, pp. 10 357–10 377, 2021.
- [24] P. Long, T. Fan, X. Liao, W. Liu, H. Zhang, and J. Pan, "Towards optimally decentralized multi-robot collision avoidance via deep reinforcement learning," in *2018 IEEE International Conference on Robotics and Automation (ICRA)*, 2018, Conference Proceedings, pp. 6252–6259.
- [25] T. Fan, P. Long, W. Liu, and J. Pan, "Distributed multi-robot collision avoidance via deep reinforcement learning for navigation in complex scenarios," *The International Journal of Robotics Research*, vol. 39, no. 7, pp. 856–892, 2020.
- [26] L. Dong, Z. He, C. Song, and C. Sun, "A review of mobile robot motion planning methods: from classical motion planning workflows to reinforcement learning-based architectures," *J. Syst. Eng. Electron.*, vol. 34, no. 2, pp. 439–459, 2023.
- [27] K. N. McGuire, C. De Wagter, K. Tuyls, H. J. Kappen, and G. de Croon, "Minimal navigation solution for a swarm of tiny flying robots to explore an unknown environment," *Sci. Robot.*, vol. 4, no. 35, p. 14, 2019.
- [28] P. Anderson, A. Chang, D. S. Chaplot, A. Dosovitskiy, S. Gupta, V. Koltun, J. Kosecka, J. Malik, R. Mottaghi, M. Savva, and A. R. Zamir, "On evaluation of embodied navigation agents," arXiv, 2018.
- [29] P. E. Hart, N. J. Nilsson, and B. Raphael, "A formal basis for the heuristic determination of minimum cost paths," *IEEE Transactions on Systems Science and Cybernetics*, vol. 4, no. 2, pp. 100–107, 1968.